Received: 29 June 2021 | Revised: 3 November 2021 | Accepted: 7 November 2021

DOI: 10.1002/hbm.25719

RESEARCH ARTICLE

WILEY

Functional magnetic resonance imaging responses during perceptual decision-making at 3 and 7 T in human cortex, striatum, and brainstem

Olympia Colizoli[1,2,3] | **Jan Willem de Gee**[1,2] | **Wietske van der Zwaag**[4] | **Tobias H. Donner**[1,2,5]

[1]Section Computational Cognitive Neuroscience, Department of Neurophysiology and Pathophysiology, University Medical Center Hamburg-Eppendorf, Hamburg, Germany

[2]Department of Psychology, University of Amsterdam, Amsterdam, The Netherlands

[3]Donders Institute for Brain, Cognition and Behaviour, Radboud University Nijmegen, Nijmegen, The Netherlands

[4]Spinoza Centre for Neuroimaging, Amsterdam, The Netherlands

[5]Amsterdam Brain and Cognition, University of Amsterdam, Amsterdam, The Netherlands

Correspondence
Olympia Colizoli, Donders Centre for Cognition, Radboud University Nijmegen, Thomas van Aquinostraat 4, 6525 GD Nijmegen, The Netherlands.
Email: olympia.colizoli@donders.ru.nl

Tobias H. Donner, Department of Neurophysiology and Pathophysiology, University Medical Center Hamburg-Eppendorf, N43, Martinistraße 52, 20246 Hamburg, Germany.
Email: t.donner@uke.de

Funding information
This research was funded by the European Union Seventh Framework Programme (FP7/2007-2013) under grant agreement No. 604102 (Human Brain Project) (to T. H. D.), and the Deutsche Forschungsgemeinschaft (DFG, German Research Foundation) DO 1240/3-1, DO 1240/2-1, and SFB 936/A7 (to T. H. D.).

Abstract

While functional magnetic resonance imaging (fMRI) at ultra-high field (7 T) promises a general increase in sensitivity compared to lower field strengths, the benefits may be most pronounced for specific applications. The current study aimed to evaluate the relative benefit of 7 over 3 T fMRI for the assessment of responses evoked in different brain regions by a well-controlled cognitive task. At 3 and 7 T, the same participants made challenging perceptual decisions about visual motion combined with monetary rewards for correct choices. Previous work on this task has extensively characterized the underlying cognitive computations and single-cell responses in cortical and subcortical structures. We quantified the evoked fMRI responses in extrastriate visual cortical areas, the striatum, and the brainstem during the decision interval and the post-feedback interval of the task. The dependence of response amplitudes on field strength during the decision interval differed between cortical, striatal, and brainstem regions, with a generally bigger 7 versus 3 T benefit in subcortical structures. We also found stronger responses during relatively easier than harder decisions at 7 T for dopaminergic midbrain nuclei, in line with reward expectation. Our results demonstrate the potential of 7 T fMRI for illuminating the contribution of small brainstem nuclei to the orchestration of cognitive computations in the human brain.

Abbreviations: 2AFC, two-alternative forced-choice; ACC, anterior cingulate cortex,; BOLD, blood oxygenation level dependent; EPI, echo-planar images; fMRI, functional magnetic resonance imaging; FSL, fMRIB software library; FWE, family-wise error rate; HRF, hemodynamic response function; IPS01, intraparietal sulcus regions 0 and 1; LC, locus coeruleus; MNI, Montreal Neurological Institute; MRI, magnetic resonance imaging; MT+, human medial temporal area; NAc, nucleus accumbens; RETROICOR, retrospective image correction technique; RF, radio frequency; ROI, region of interest; SN, substantia nigra; SNR, signal-to-noise ratio; T, Tesla; TFCE, threshold-free cluster enhancement; tSNR, temporal SNR; V1, primary visual cortex; V3AB, third visual cortex regions A and B; VTA, ventral tegmental area.

Wietske van der Zwaag and Tobias H. Donner shared senior authors.

KEYWORDS
7 T fMRI, brainstem, perceptual decision-making, reward, ultra-high field, ventral tegmental area

1 | INTRODUCTION

The last decade has shown significant progress in ultra-high field (UHF) magnetic resonance imaging (MRI), providing excellent image quality and sub-millimeter resolution for functional, structural, and connectivity images. 7 T MRI is on its way to becoming a user-friendly modality, with sequence development centered around increasing spatial and temporal resolution, as well as improving the spatial specificity of the blood oxygenation level-dependent (BOLD) signal for studies of brain function (for a review, see van der Zwaag, Schäfer, Marques, Turner, & Trampel, 2016). Accordingly, 7 T functional MRI (fMRI) is progressively used to study brain functions including perception, motor action, decision-making, language, and emotion in normal subjects (e.g., Bode et al., 2011; Harvey, Klein, Petridou, & Dumoulin, 2013; Hayashi, van der Zwaag, Bueti, & Kanai, 2018; Mestres-Missé, Turner, & Friederici, 2012; Theysohn et al., 2013; Thürling et al., 2011, 2012; Torrisi et al., 2018; van der Zwaag, Da Costa, Zürcher, Adams, & Hadjikhani, 2012). Given the increasing availability of 7 T MRI scanners, an important question facing researchers is which fMRI applications benefit most from 7 T fMRI, compared to more standard (cheaper and more widely available) measurements at 3 T.

In general, 7 T is expected to improve the image signal-to-noise ratio (SNR) of MRI measurements relative to standard 3 T acquisitions (Edelstein, Glover, Hardy, & Redington, 1986; Pohmann, Speck, & Scheffler, 2016). For BOLD fMRI, this predicts stronger evoked fMRI responses (Turner et al., 1993; van der Zwaag et al., 2009; Yacoub et al., 2001). Yet, increased field strength is also accompanied by an increase in susceptibility-induced distortions, such as air–water interfaces and the contributions from physiological noise (Triantafyllou et al., 2005; van der Zwaag et al., 2016). Physiological (cardiac and respiratory) noise is greater in the brainstem than in the cortex (Harvey et al., 2008). Given the above-described trade-offs, fMRI at 7 T is not necessarily always preferable to fMRI at 3 T.

Previous studies have used block designs with passive sensory stimulation or basic motor tasks to assess the advantages of 7 T for BOLD-fMRI measurements (e.g., Duong et al., 2002; Schäfer et al., 2007; van der Zwaag et al., 2009; Yacoub et al., 2001, 2003). Other studies have compared 7 and 3 T fMRI for clinical applications (e.g., Beisteiner et al., 2011; Morris et al., 2019) or investigated task-evoked activation related to cognition (de Hollander, Keuken, van der Zwaag, Forstmann, & Trampel, 2017;Theysohn et al., 2013; Torrisi et al., 2018). Only some of these studies have been direct head-to-head comparisons between functional measurements at the two field strengths in the same individuals (e.g., Schäfer et al., 2007; van der Zwaag et al., 2009). Furthermore, studies have either focused on the cerebral cortex or did not explicitly discriminate between cortical and subcortical brain regions in the field-strength comparisons. Few studies have quantified the benefit in sensitivity for examining cognitive functions by taking (full) advantage of the greater field strength and in light of the inherent limitations (Theysohn et al., 2013; Torrisi et al., 2018).

One part of the brain, for which 7 T fMRI might prove to be particularly beneficial over 3 T fMRI is the brainstem. The brainstem is made up of a multitude of small nuclei, precise delineation of which requires higher spatial resolution than for cortical or even other subcortical regions (e.g., the striatum). Despite successful attempts using sophisticated measurement protocols (D'Ardenne, McClure, Nystrom, & Cohen, 2008;de Gee et al., 2017; Iglesias et al., 2013), the brainstem is notoriously difficult to image with 3 T fMRI. At the same time, the brainstem is an important target for cognitive (de Gee et al., 2017; Iglesias et al., 2013) and translational (Stephan, Iglesias, Heinzle, & Diaconescu, 2015) neuroimaging. This is because the brainstem houses the nuclei of the brain's so-called neuromodulatory (e.g., dopamine or noradrenaline) systems, which send widespread, ascending projections to higher parts of the brain including the cerebral cortex and seem to play a key role in cognition and disturbances thereof (Aston-Jones & Cohen, 2005; Dayan, 2012; Montague, Hyman, & Cohen, 2004).

The purpose of the current study was to directly compare the two field-strength acquisitions, within the same individuals, in the context of a typical cognitive neuroimaging experiment. To this end, we used a well-established behavioral task that simultaneously assesses multiple cognitive operations including: perceptual processing, decision-making, action selection, as well as feedback/reward processing. We focused our comparison on a range of select brain regions, including motion-responsive visual cortical regions and anterior cingulate cortex (ACC), the striatum, and the noradrenergic locus coeruleus (LC) as well as dopaminergic ventral tegmental area (VTA) and substantia nigra (SN). We used a direct head-to-head analysis of task-evoked fMRI responses (as well as the temporal SNR [tSNR] of ongoing signal fluctuations) within the same healthy adult participants scanned at 3 and 7 T. The neurophysiological underpinnings of the different components of task-evoked neural responses in our task have been well-characterized in the above structures by previous single-unit physiology in rodents and monkeys. We compared a successful 3 T fMRI protocol previously used to investigate small midbrain structures (de Gee et al., 2017) with a suitably adapted protocol for 7 T fMRI (Marques & Norris, 2018), given both the potential for reducing partial-volume effects and the inherent limitations of greater field-strength acquisitions.

2 | METHODS

We acquired fMRI (near-whole-brain coverage) and behavioral data in a 3 and a 7 T setup from healthy adult volunteers who performed a

two-alternative forced-choice (2AFC) motion discrimination task with monetary-coupled feedback. Independent analyses of the relationship of choice behavior and participants' pupil responses during the 3 T sessions have been published previously (Colizoli, de Gee, Urai, & Donner, 2018; de Gee et al., 2017). The analyses presented in the current paper are conceptually and methodologically distinct. Relevant methods that have previously been published are again summarized in Section 2.

2.1 | Participants

All participants were screened for MRI-related health risks using a standard procedure and gave written informed consent. The experiment was approved by the Ethical Committee of the Department of Psychology at the University of Amsterdam. Participants were financially compensated with €10 per hour in the behavioral lab and €15 per hour for MRI scanning. In addition to this standard compensation, participants earned money on the 2AFC task based on their performance within each scan session: €0–10 linearly spaced from 50% to 100% accuracy for each scan session (i.e., 50% correct = €0, 75% = €5, 100% = €10). At the end of each 2AFC run (25 trials, see Section 2.3), participants were shown (on screen) their average performance accuracy across the runs in the current session and their corresponding monetary reward.

Ten participants (two authors) completed both the 3 and 7 T MRI measurements. Due to technical failure, physiological recordings were lost during the 7 T acquisition for more than 50% of the data of two participants and for six individual runs (across three participants). These two participants were, therefore, excluded from further analysis. This yielded a sample of eight participants (including one author; 3 women, $M = 28$ years, $SD = 4.8$, range 23–37), in which we performed the head-to-head comparison reported in this article.

The 3 T acquisition data from one session of one participant were excluded from further analysis because of motion-related MRI artifacts.

2.2 | Procedure

Participants completed seven sessions in total: one behavioral session, then four 3 T MRI sessions and thereafter two 7 T MRI sessions. Each participant completed one behavioral session in order to determine individual motion discrimination thresholds (for 70% and 85% accuracy in terms of motion coherence; see Section 2.3) before completing several MRI sessions across different days. We were unable to counterbalance the acquisitions of the 3 and 7 T sessions across participants, because the 3 T study was ongoing before the 7 T study could begin. We took advantage of the additional 3 T sessions (four) as compared with the 7 T sessions (two), by splitting the 3 T data set into two subsets ("3 T-A" and "3 T-B") in order to compare the 7 T data set to a single 3 T data set (see Sections 2.3 and 2.7).

During the MRI acquisitions, participants lay supine in the scanner, and their heads were secured with additional padding to minimize motion. Participants wore ear protection and headphones and were instructed to maintain a central fixation during all functional runs. The cardiac cycle was monitored with the vendor-provided pulse oximeter attached to the left ring finger. Respiratory activity was recorded with a vendor-provided chest belt. Physiological signals were recorded at a sampling rate of 496 Hz. Stimuli were presented on a 31.55 in. MRI compatible LCD display (BOLD screen, Cambridge Research Systems, UK) with a spatial resolution of 1,920 × 1,080 pixels and a refresh rate of 120 Hz.

2.2.1 | 3 T MRI experiment

Participants viewed the projection screen from 120 cm via a mirror attached to the head coil. Sessions began with reference and anatomical scans, during which participants practiced the 2AFC motion discrimination task (1–2 blocks of 50 trials). Participants were administered six runs of the 2AFC task during each scan session. After the sixth run, a B0-field map was acquired. A coherent-motion localizer was administered at the end of the scan session (Section 2.9). Each session took 2 hr. Participants completed four sessions across different days.

2.2.2 | 7 T MRI experiment

Participants viewed the projection screen from 208 cm via a mirror attached to the head coil. Sessions began with reference scans, during which participants practiced the 2AFC motion discrimination task (1–2 blocks of 50 trials). Participants were administered six runs of the 2AFC task during each scan session. After the sixth run, a B0-field map was acquired. A coherent-motion localizer was administered at the end of the scan session. Each session took 1.5 hr. Participants completed two sessions across different days.

2.3 | 2AFC motion discrimination task

The methods of the 2AFC motion discrimination task have been previously described in detail in (Colizoli et al., 2018). Stimuli were presented using the Psychophysics Toolbox extensions as part of MATLAB version 2012b (Brainard, 1997). Participants were asked to decide whether the net direction of motion of a dynamic random dot kinematogram (presented for 750 ms) was upward or downward (indicated via button press with the left or right index finger; response mappings were counterbalanced across participants); the ratio of coherently moving "signal dots" to incoherently moving "noise dots" determines the difficulty level on each trial (hard or easy, 70% vs. 85% correct, respectively). The motion coherence levels corresponding to these two difficulty (i.e., performance) levels were individually determined using a staircase procedure with seven levels (100 trials per

level, 50 trials per visual hemifield, levels were: 0%, 2.5%, 5%, 10%, 20%, 40%, and 80% coherence) in a separate behavioral session that took place before the MRI sessions. Motion coherence onset was indicated by both a visual cue (change of fixation region) and auditory cue (pure tone or white noise). In the current study, we were not interested in the effect of the auditory cue. During the 2AFC task, motion coherence varied randomly from trial-to-trial so that observers performed at 70% correct in 2/3 of trials ("hard") and at 85% correct in one-third of trials ("easy"). After a variable delay following the choice on each trial (3.5–11.5 s, uniformly distributed across five levels, steps of 2 s), feedback was presented (green fixation square for correct, red for error, 0.42 s) that was coupled to a monetary reward (see Section 2.1 for details). The intertrial interval lasted 3.5–11.5 s, uniformly distributed across five levels, steps of 2 s. During all phases of a trial, with the exception of the stimulus presentation of coherent motion, random dot motion (0% coherence) was presented.

All stimuli were presented within a central annulus (not visible to participants). The annulus contained 524 dots all within one visual hemifield (left or right; counterbalanced across runs and participants). The different screen-viewing distances between the two scanner environments (see Section 2.2) caused some differences in the visual stimulation parameters: The annulus' outer diameter was 16.8° or 9.4° and dots moved at 7.5°/s or 3.9°/s during the 3 or 7 T acquisitions, respectively. We note that the bore of the 7 T scanner used in the current study was longer than that of the 3 T scanner, restricting the maximum visual angle of the stimulus given our specific stimulus setup.

One run of the 2AFC task contained 25 trials. Subjects performed twice as many sessions at 3 T than at 7 T (see Section 2.1); therefore, we split the 3 T data into two subsets (3 T-A and 3 T-B; see Section 2.6) with 6–12 runs distributed over 1–2 sessions, yielding a total of 150–300 trials per 3 T subset per participant. For the 7 T acquisition, 6–12 runs distributed over 1–2 sessions were included in the analysis, yielding a total of 150–300 trials per participant. Note that one participant only had three (usable) sessions of 3 T data.

2.4 | MRI data acquisition at 3 T

MRI data were acquired on a 3 T Philips Achieva XT MRI scanner (Amsterdam, the Netherlands) using a 32-channel dStream head coil across four sessions. Single-shot, 2D gradient echo-planar images (EPI) were acquired in 33 slices oriented perpendicular to the floor of the fourth ventricle and to the longitudinal extent of the LC (Keren, Lozar, Harris, Morgan, & Eckert, 2009): 2 × 2 mm in-plane resolution, 3 mm slice thickness (no gaps), FOV 192 × 192 × 99 mm. TR = 2 s; echo time [TE] = 27.62 ms; flip angle = 76.1°; SENSE acceleration factor = 3.0; bandwidth = 2,213 Hz/pixel. A structural T1-weighted scan was acquired for anatomical co-registration (voxel size: 1 × 1 × 1 mm^3, TR = 8.13 ms, TE = 3.7 ms, flip angle = 8°). A B0-field map was acquired for unwarping (voxel size: 2 × 2 × 2 mm^3, TR = 10.85 ms, TE = 3.03, flip angle = 8°). Slices were acquired sequentially in the ascending (foot to head) direction.

We chose anisotropic voxels and the above orientation of the imaging volume for EPI to optimize spatial sampling for the LC (for details, see de Gee et al., 2017). The LC is an elongated structure with small diameter (a few millimeters) and comparably large longitudinal extent (~15 mm) along the floor of the fourth ventricle (Betts et al., 2019). The rationale was that the LC was the smallest brainstem nucleus to be assessed here.

2.5 | MRI data acquisition at 7 T

MRI data were acquired on a 7 T Philips Achieva MRI scanner (Amsterdam, the Netherlands) using a 32-channel Nova head coil across two sessions. Gradient EPIs were acquired in 30 slices oriented perpendicular to the floor of the fourth ventricle: 1.5 × 1.5 mm in-plane resolution, 3 mm (no gaps) slice thickness, FOV 192 × 192 × 90 mm. The voxel size was reduced in the in-plane direction compared to the 3 T acquisition, again because of the geometry of the LC described in Section 2.4. This way, the higher SNR at 7 T was traded for resolution. TR = 2 s; TE = 23 ms; flip angle = 70°; SENSE acceleration factor = 2.5; bandwidth = 1,652 Hz/pixel. The TE and flip angle of the EPI differed from those in the 3 T protocol to accommodate for the shorter T_2^* and longer T_1 at 7 T. Finally, a B0-field map was acquired for unwarping (voxel size: 2 × 2 × 2 mm^3, TR = 4.6 ms, TE = 1.88, flip angle = 10°). Slices were acquired in the ascending (foot to head) direction in an interleaved fashion (first odd then even slices).

2.6 | fMRI preprocessing

Preprocessing steps were identical for the 3 and 7 T acquisitions. Each run of the EPI images was (a) brain extracted using the BET tool as part of FSL version 5.0.2.1 (Jenkinson, Beckmann, Behrens, Woolrich, & Smith, 2012; Smith et al., 2004; Woolrich et al., 2009); (b) unwarped based on the session-specific B0-field map (FUGUE, FSL); (c) motion corrected (sinc interpolation, MCFLIRT, FSL); and (d) high-pass filtered to correct for low-frequency drifts (Gaussian-weighted least-squares straight line fitting, window size = 50 samples).

A single reference image for all EPI-based registration, including motion correction, was defined for each session as: the motion-corrected mean volume of the third run (out of six) of the 2AFC task. The reference image of each session was transformed to the T1-weighted MNI-152 2-mm space, via the subject-specific T1-weighted anatomical image, using an affine transformation with 12 degrees of freedom, the normmi cost function, and sinc interpolation (FLIRT, FSL). The registration to standard space of each participant's session (at each field strength) was checked visually. An example registration in T1-weighted MNI-152 2-mm space is shown in Supplementary Figure 1. We verified that the choice of registration method had only a negligible effect on the results (affine vs. nonlinear registration; see Supplementary Figure 2).

Within each session, all EPI runs were subsequently concatenated in time. Nuisance regression was applied to the concatenated EPI runs for each session separately, including physiological noise correction in which cardiac and respiratory phases were assigned separately for each slice in the concatenated EPI time series (an extended version of RETROICOR; PNM, FSL) (Brooks, Faull, Pattinson, & Jenkinson, 2013; Glover, Li, & Ress, 2000). Nuisance regressors included 34 physiological signal components and the mean signal fluctuation within the fourth ventricle. The fourth ventricle was manually defined by marking voxels on the basis of the T1-weighted MNI-152 2-mm space (52 voxels) and transformed to the subject- and session-specific 3D space (FLIRT). Finally, slice-timing correction was applied after physiological noise removal. This preprocessing order was implemented because the RETROICOR entails separate physiological noise regressors for each slice to ensure a precise temporal alignment between the measured respiration and cardiac cycles and the slice-acquisition times. Indeed, previous work established that temporal *SD* (of simulated and resting-state data) is most reduced when volume registration (e.g., motion correction) is done before RETROICOR and slice-timing correction is done after RETROICOR (Jones, Bandettini, & Birn, 2008). The slice-time corrected residuals of the nuisance regression were transformed to the T1-weighted MNI-152 2-mm space and used in the subsequent analyses. Finally, whole-brain analyses were restricted spatially by the common field of view between the two field-strength acquisitions.

No run-related nuisance regressors were included in the nuisance regression. This procedure will leave offsets at the transitions between runs, thus introducing transients in the concatenated-session data that remained unaccounted for in our analyses. We minimized this problem in our preprocessing: we applied high-pass filtering separately to the time series on each run to remove low-frequency drifts. Additionally, session-specific nuisance regressors were included in the task-evoked general linear models (GLMs; see Section 2.7). Furthermore, and critically, the preprocessing steps and GLM analysis was identical between field-strength acquisitions.

Linear regression of the physiological noise components may not suffice to fully remove their effects, or this approach may remove a disproportional amount of noise at certain field-strength acquisitions and within certain brain regions (Beissner, 2015; Sclocco, Beissner, Bianciardi, Polimeni, & Napadow, 2018). To minimize this issue, we did not use any spatial smoothing in the region of interest (ROI) analyses, as suggested by Beissner, Schumann, Brunn, Eisenträger, and Bär (2014). Furthermore, we also quantified residual noise fluctuations in the vicinity of the brainstem using the fourth ventricle ROI and removed those from the data in the same nuisance regression as the RETROICOR.

We chose to conduct the main analyses in standard space (as opposed to native space) to do whole-brain comparisons, to work with a single (equal) voxel resolution across field-strength acquisitions (see Sections 2.4 and 2.5), and to make the results comparable to cognitive neuroscience studies (which often report results in a standard space).

2.7 | Quantifying task-evoked BOLD responses

The preprocessed time series were entered into a GLM using FEAT version 6.0 (FSL v. 5.0.2.1). For each participant, a GLM was fit to each of their data sets (3 T-A, 3 T-B, and 7 T). Session data were concatenated within each data set (one to two sessions per data set per participant). The number of trials entered into each GLM was equalized across data sets for each participant according to the minimum of either the 3 T-A, 3 T-B, or 7 T acquisitions. Regressors of interest were the following: two regressors modeled the easy and hard trials for the responses during the decision interval (time-locked to the onset of the dot-motion stimulus). The easy and hard stimulus regressors were parametrically modulated by reaction time (RT). Two regressors modeled the responses during the feedback interval for correct and error trials (time-locked to the onset of the visual feedback). Nuisance regressors included one regressor for missed trials (stimulus and feedback responses were combined), and one to two regressors (each) modeling a session's mean value. All regressors were convolved with the double-gamma hemodynamic response function and high-pass filtered (cut-off at 100 s). Grand-mean intensity normalization was applied to the entire 4D data set by a single multiplicative factor. The statistical analysis of the time-series was carried out using FILM with local autocorrelation correction (Woolrich, Ripley, Brady, & Smith, 2001). Contrasts of interest were the following: (a) the stimulus response (easy + hard trials > implicit baseline), (b) the feedback response (correct + error trials > implicit baseline), (c) the hard > easy stimulus response, and (d) the error > correct feedback response.

Within each ROI (see Section 2.8) and for each contrast of interest, the task-evoked responses were averaged using a weighted sum, separately for each data set. Subsequently, the t-statistics from the 3 T-A and 3 T-B data sets were averaged in order to compare the 7 T data set to a single 3 T data set. For each contrast of interest, differences in t-statistics were evaluated in a two-way repeated-measures analysis of variance (ANOVA) with factors ROI group (levels: cortical regions, striatum, and brainstem nuclei) and field strength (levels: 3 vs. 7 T) using the Python package *pyvttbl*. Planned comparisons for ROIs were done by means of a nonparametric two-tailed permutation test (10,000 permutations, custom Python code; (Efron & Tibshirani, 1998; Ernst, 2004). No spatial smoothing was applied for the ROI analyses (Beissner et al., 2014).

At the whole-brain level, field-strength differences for each contrast of interest were investigated separately. The resulting t-statistic of the GLM fits for the 3 T-A and 3 T-B data sets were averaged in order to compare the 7 T data set to a single 3 T data set. Task-evoked responses were formally tested by means of a nonparametric one-sample permutation test with 5,000 permutations and variance smoothing (5 mm), separately for the positive and negative directions (randomize, FSL). Variance smoothing was applied to the t-maps, as per recommendation by FSL for small samples (<20). The family-wise error rate (p-value threshold = .05) was controlled using the threshold-free cluster enhancement method (FSL). The same procedure was applied to test the 3 T-A and 3 T-B data sets separately.

2.8 | Defining ROIs

A substantial body of previous electrophysiology work on variants of our behavioral task has identified neural correlates of different elementary operations entailed in the task in several cortical and subcortical brain regions, specifically: sensory encoding, decision-making, reward anticipation, and reward feedback processing (e.g., Britten, Shadlen, Newsome, & Movshon, 1992; de Gee et al., 2017; Ding & Gold, 2013; Donner et al., 2007; Lak, Nomoto, Keramati, Sakagami, & Kepecs, 2017; Rees, Friston, & Koch, 2000; Siegel, Donner, Oostenveld, Fries, & Engel, 2006; Urai, Braun, & Donner, 2017). We thus defined a number of ROIs a priori, based on their involvement in the above task-related operations: Dorsal visual cortical regions based on probabilistic maps of visual topography (Wang, Mruczek, Arcaro, & Kastner, 2014) included area hMT (hereafter referred to as MT+), V1, V3AB, and intraparietal sulcus regions 0 and 1 (IPS01); the ACC was based on the Harvard-Oxford Cortical Atlas (FSL). The corpus striatum regions included the caudate, putamen, and nucleus accumbens (NAc), based on the Oxford-GSK-Imanova Structural–anatomical Striatal Atlas (FSL). Neuromodulatory brainstem nuclei included the VTA (Ballard et al., 2011), SN (Murty et al., 2014), and LC (Keren et al., 2009). Additionally, three "ROI groups" were defined as the average (t-statistic) of the following combinations of individual ROIs: V1, V3AB, MT+, IPS01, and ACC ("cortical regions"); caudate, putamen, and NAc ("striatum"); and LC, SN, and VTA ("brainstem nuclei").

All ROI masks used here were probabilistic. To obtain an unbiased probability value in the combined masks (dorsal with ventral parts of V1, V3A with V3B, and IPS0 with IPS1), the probability values in overlapping voxels were averaged. For all ROIs, we combined homotopic regions in both hemispheres into a single ROI. All ROI masks were restricted spatially by the common field of view between the 3 and 7 T acquisitions. Finally, within each ROI mask, the probability values were rescaled to be between 0 and 1. The means within each ROI mask were weighted based on these rescaled probability values (using all voxels within each ROI).

Note that we used an existing and validated probabilistic atlas for area MT+ in order to ensure that all ROI masks used in the comparison across brain regions were based on independent (probabilistic) atlases from the literature. The coherent-motion localizer task was not used to delineate these motion-responsive visual cortical areas, but rather to quantify their fMRI responses at both field strength using a well-established protocol.

2.9 | Coherent-motion localizer

We aimed to verify that the atlas-based V3AB and MT+ ROIs responded significantly to coherent motion as compared with random motion (Braddick et al., 2001; Britten, Shadlen, Newsome, & Movshon, 1993; Newsome & Pare, 1988). To this end, we also ran so-called motion localizer runs, in which blocks of random dot kinematograms at 100% motion coherence were alternated with blocks of random dot kinematograms at 0% coherence. Each block lasted 10 s and showed either coherent dot motion in a single direction or random motion. Eight directions of coherent motion were presented twice each in randomized order (four cardinal and four ordinal directions). In total, 32 blocks were presented per run of the localizer. The order of the coherent and random motion blocks was counterbalanced both within and across participants (i.e., ABAB- > BABA). To control attention and minimize eye movements, participants were instructed to push a button with their right index finger whenever the fixation region changed from gray to green. A change in the fixation region occurred during half of the blocks at random, with the constraint that it occurred an equal number of times during the coherent motion and random motion blocks. Button-press responses were not analyzed. Within a block, the color-change in fixation occurred at random between 1 and 8 s. Motion parameters were the same as indicated for the motion discrimination task at the corresponding MRI field strength with the exception that the dots were presented within the full annulus (not in one half of the visual field). One run of the localizer was administered during each scan session (in total four runs for 3 T and two runs for 7 T acquisitions) and lasted 5.7 min.

Preprocessing steps for the motion localizer runs were as follows. Each run was (a) brain extracted using the BET; (b) unwarped based on the session-specific B0-field map; (c) motion corrected (sinc interpolation, MCFLIRT, FSL); and (d) high-pass filtered to correct for low frequency drifts (Gaussian-weighted least-squares straight line fitting, window size = 50 samples). For each session, one EPI volume, the motion-corrected mean volume of the third run (out of six) of the 2AFC task, was used as the reference image for all EPI-based registration including motion correction.

The statistical analysis was carried out using FEAT version 6.00 (FSL). At the first-level analysis, two regressors of interest were modeled for each run: coherent and random motion. The contrast of coherent > random motion was of interest. Time-series statistical analysis was carried out using FILM with local autocorrelation correction. At the second level, the contrast estimates of two runs from each field-strength acquisition (3 and 7 T) were averaged for each participant. Statistic images (z-statistic) were thresholded at $p < .05$ uncorrected for multiple comparisons. The mean z-statistic in each ROI was weighted based on the probability values of the ROI masks. Coherent-motion responses for each field-strength acquisition within each individual ROI were tested against zero by means of a nonparametric two-tailed permutation test (10,000 permutations, custom Python code).

Note that because the visual angles differed between field-strength acquisitions, we could not formally test for differences in the BOLD-acquisition sensitivity of MT+ based on the localizer (Born & Bradley, 2005).

3 | RESULTS

The current study compared evoked responses of 3 and 7 T fMRI acquisitions for a number of select brain regions in visual cortex,

striatum and brainstem, within the same healthy adult participants. We used an fMRI acquisition and analysis protocol, with which we have succeeded in detecting and characterizing brainstem responses during perceptual decision-making at 3 T (de Gee et al., 2017) and adapted this protocol to take advantage of the potential benefits of higher-resolution scanning at 7 T. At both field strengths (3 and 7 T), we measured fMRI responses with near-whole-brain coverage, while participants performed a visual choice task (random dot-motion discrimination), followed by the monetary reward-coupled feedback (Figure 1a). Two difficulty levels were randomly intermixed so that each trial was either relatively hard (70% correct) or relatively easy (85% correct), depending on individual-threshold motion-coherence levels that were established in a behavioral session before scanning began (Figure 1b). This ensured a high level of behavioral control and minimized session-to-session as well as subject-to-subject variation in performance and cognitive effort. The task entailed several operations with well-characterized neural substrates (Gold & Shadlen, 2007): encoding of visual motion information, perceptual decision-making, decision confidence, and/or reward anticipation during and right after decision formation; and processing of reward prediction errors upon the delivery of decision outcome in terms of visual feedback.

All participants took part in four 3 T MRI sessions and then two 7 T MRI sessions (Figure 1b). As expected, participants' choices were faster and more accurate in the easy compared to the hard condition of the discrimination task (Figure 1c,d). Each individual performed at higher accuracy for the hard than for the easy condition in each scanning session (data not shown). Critically, RT and accuracy were very similar in the two scanner environments (Figure 1c,d; no significant

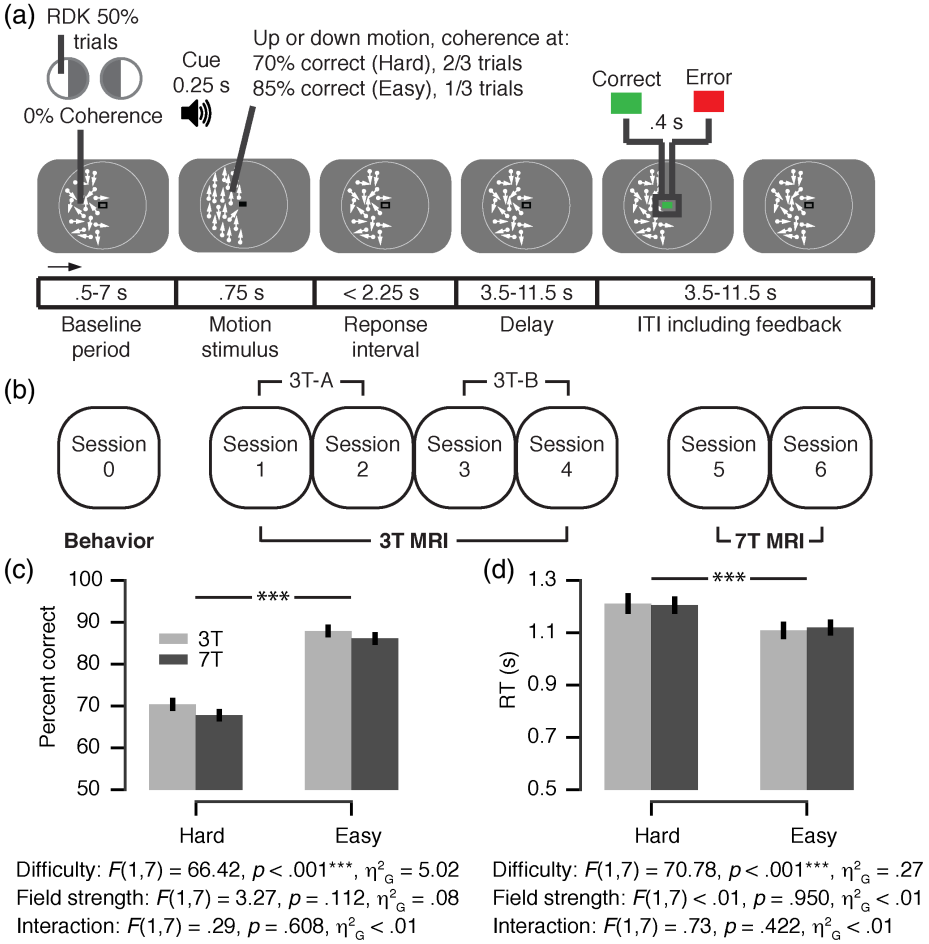

Difficulty: $F(1,7) = 66.42$, $p < .001^{***}$, $\eta^2_G = 5.02$
Field strength: $F(1,7) = 3.27$, $p = .112$, $\eta^2_G = .08$
Interaction: $F(1,7) = .29$, $p = .608$, $\eta^2_G < .01$

Difficulty: $F(1,7) = 70.78$, $p < .001^{***}$, $\eta^2_G = .27$
Field strength: $F(1,7) < .01$, $p = .950$, $\eta^2_G < .01$
Interaction: $F(1,7) = .73$, $p = .422$, $\eta^2_G < .01$

FIGURE 1 Experimental design and behavior. (a) Behavioral task. Subjects performed a two-alternative forced-choice (2AFC) motion-direction (up/down) discrimination task during functional magnetic resonance imaging (fMRI). Random dot kinematograms (RDK) were shown in one visual hemifield on each run (hemifields alternated sides across runs). The decision interval ranged from onset of the motion stimulus to the participant's response. The feedback interval ranged from feedback onset into the subsequent intertrial interval (ITI). Feedback was coupled to a monetary reward based on the average accuracy of runs of 25 trials. (b) Experimental protocol. Participants completed seven sessions in total: one behavioral session, then four 3 T MRI sessions and finally two 7 T MRI sessions. The data of the two 7 T sessions were averaged. The 3 T MRI data was split into two subsets, 3 T-A and 3 T-B, and averaged (i.e., "3 T") in order to compare the 7 T to a single data set. (c,d) Choice accuracy (c) and mean reaction time (RT) (d) as a function of task difficulty and field strength (repeated measures two-way analysis of variance [ANOVA]). F-statistics, main effect of task difficulty, field strength, and their interaction. $^{***}p < .001$ (ANOVA results). Error bars, *SEM* ($N = 8$). Panel (a) is reproduced from Colizoli et al. (2018)

main effect of field strength, and no significant interaction between task difficulty and field strength. A detailed quantification of participants' behavior and accompanying pupil responses (for 3 T data only) is presented in (Colizoli et al., 2018).

3.1 | Comparison of evoked responses at 3 and 7 T for different brain regions

We analyzed evoked fMRI responses within a number of cortical and subcortical brain regions that are implicated in different operations engaged in the visual motion discrimination task (sensory encoding, decision-making, decision certainty/reward anticipation, feedback processing) (Britten et al., 1992; de Gee et al., 2017; Ding & Gold, 2013; Donner et al., 2007; Lak et al., 2017; Rees et al., 2000; Siegel et al., 2006; Siegel, Engel & Donner, 2011; Urai et al., 2017): (a) cortex: three (clusters of) cortical areas along the dorsal pathway analyzing visual motion (V1, V3AB, MT+) or involved in task/decision processing (IPS01 and ACC); (b) the corpus striatum (caudate nucleus, putamen, NAc); and (c) brainstem: three modulatory nuclei in the pons midbrain, all of which contribute to decision-making, but whose activity is notoriously difficult to measure at 3 T, the noradrenergic LC, and the dopaminergic SN and VTA.

We first verified that an established pattern of sensory responses in visual cortex was present in our data. In separate localizer runs (see Section 2), we found that extrastriate visual cortical regions V3AB and MT+, but not V1, exhibited the sensory responses specific to coherent compared to incoherent dot motion expected from previous work (Huk, Dougherty, & Heeger, 2002; Tootell et al., 1995, 1997). This was true and robust for both field strengths (Figure 2; all *p*-values < .05). Please note that the voxel size and the size of the visual stimulus were both smaller at 7 than 3 T (both factor of ~1.8, see Section 2). Smaller voxels and smaller stimuli (driving a smaller portion of the retinopically organized visual cortical areas (Huk & Heeger, 2002; Wang et al., 2014) are both expected to reduce overall fMRI responses in these cortical regions. At the same time, smaller voxels may increase signal responses due to a reduction of partial volume effects. We found about equally strong (statistically indistinguishable, all *p*-values > .2) responses in both V3AB and MT+. Therefore, either the difference in retinotopic stimulation between acquisitions was nonsignificant, or the smaller voxels of the 7 T acquisition compensated for the retinotopic stimulation differences due to a decrease in partial volume effects. We are not able to distinguish between these two scenarios based on the MT localizer data alone (see the Supplementary Materials, Supplementary Figures 3 and 4 for an analysis of tSNR). During the motion discrimination task, we also found high across-session overlap of the responses in visual cortex at 3 T, which were performed in four different sessions (Supplementary Figure 5).

Having thus established the quality of our data, we grouped the brain regions into three groups listed above (cortical regions, striatum, and brainstem nuclei), for which we expected differential BOLD-acquisition sensitivity on fMRI field strength. Please note that each of these groups consisted of precisely delineated brain regions, some of which were small (the brainstem nuclei). For each of these groups we then quantified the task-evoked responses as t-statistics (a) during the decision interval of the task (i.e., time-locked to the onset of the dot-motion stimulus; see Section 2); and (b) the post-feedback interval, time-locked to the feedback color (green or red) that informed subjects about the correctness of their preceding choice (Figure 1a). For each interval, we quantified two distinct components of the task-evoked responses: the overall response (compared to the implicit baseline) and the differential response between hard and easy decisions (decision interval) and between error and correct trials (feedback interval) (Figure 3). Planned comparisons included the interaction between ROI (group) and field strength for each contrast of interest. The parameter estimates (and *SD*s) of the contrasts of interest for each ROI (group) are presented in Supplementary Table 1.

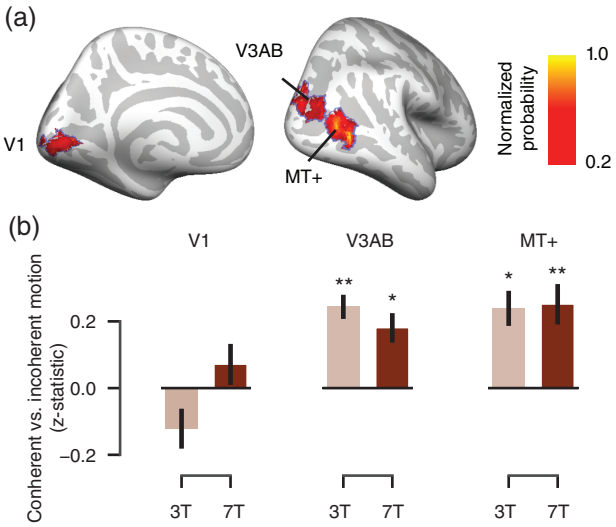

FIGURE 2 Visual cortical responses to coherent versus incoherent random dot motion (localizer runs). (a) Regions of interest (ROIs). Probabilistic mask from Wang et al. (2014) for visual cortical areas V1, V3AB, and MT+ displayed on the cortical surface, with thresholding at $p = .2$ for illustration only. Each mask was rescaled between 0 and 1 (normalized probability). (b) Differential responses to coherent (100%) relative to incoherent (0%) dot motion during the coherent-motion localizer within the probabilistic masks shown in (a) for each field strength. Coherent-motion responses for each ROI and field strength were tested against zero: $^{*}p < .05$, $^{**}p < .01$ (two-tailed permutation tests). Error bars, *SEM* ($N = 8$)

During the decision interval, we observed a significant interaction between ROI group and fMRI field strength for the overall response (Figure 3a, see Supplementary Figure 6 for the individual cortical and striatum ROIs). The field-strength difference within the cortical regions differed from that within the striatum, and a trend toward a field-strength difference was observed between the cortical regions and the brainstem nuclei (Figure 3a; $p = .069$). The biggest improvement at 7 T seemed to occur for the brainstem nuclei and smallest improvement for the cortical regions. For the hard versus easy contrast, a trend was observed for the main effect of field strength

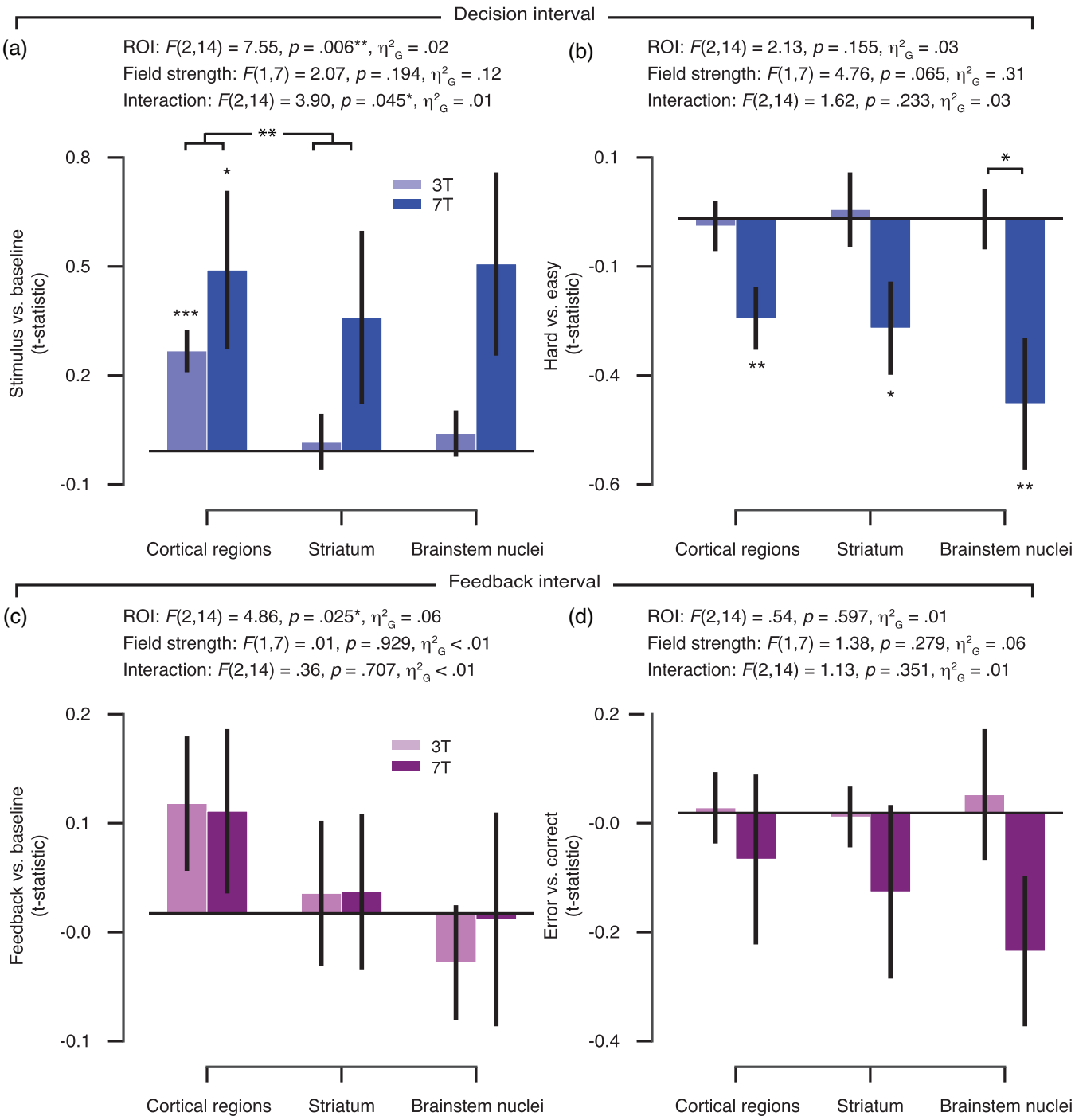

FIGURE 3 Task-evoked responses for 3 and 7 T acquisitions across cortical regions, striatum, and brainstem nuclei. (a) Amplitude of evoked response per region of interest (ROI) group (cortical regions, striatum, and brainstem nuclei) and field strength for the overall response within the decision interval (stimulus-locked and compared to the implicit baseline). (b) The amplitude difference between hard as compared with easy trials (decision interval). (c) Amplitude of evoked response per ROI group and field strength for the overall response within the feedback interval (feedback-locked and compared to the implicit baseline). (d) The amplitude difference between error as compared with correct trials (feedback interval). The 3 T amplitudes were averaged across 3 T-A and 3 T-B data subsets. Results of the repeated-measures analysis of variance (ANOVA) are given for each contrast of interest: F-statistics, main effect of ROI group, field strength, and their interaction. Planned comparisons: $^{*}p < .05$, $^{**}p < .01$, $^{***}p < .001$ (two-tailed permutation tests). Error bars, *SEM* ($N = 8$)

(Figure 3b). Although no interaction between ROI group and field strength was obtained for the comparison of hard with easy decisions, only the brainstem nuclei showed a significant field-strength difference. The pattern of effects displayed in Figure 3a,b is consistent with the idea that task-evoked responses measured at 3 T are robust in the cortical regions tested, but not in subcortical structures; while

responses measured at 7 T are more robust throughout the cortical and subcortical brain regions.

For the feedback interval, a significant main effect of ROI group was observed for the overall responses (Figure 3c). No other effects were observed for the feedback interval. Numerically, however, for the comparison of error with correct trials, the biggest improvement at 7 T seemed to occur for the brainstem nuclei (Figure 3d).

When assessing the individual brainstem nuclei (Figure 4), the pattern of data suggests a particular benefit from higher field strength. In particular, evoked differential responses during the decision interval (hard vs. easy) were significantly stronger at 7 T as compared with 3 T in the VTA and SN (Figure 4c) and during the feedback interval (error vs. correct) within the LC (Figure 4e) (all p-values < .05).

No significant differences between field strengths for the task-evoked responses were obtained at the level of the whole brain. Supplementary Figure 7 shows the number of participants who had greater or equal task-evoked responses for the 7 T as compared with the 3 T acquisition for each contrast of interest within each ROI group (Figure 3) and brainstem nuclei (Figure 4).

Finally, we investigated tSNR at the whole-brain and ROI level (see Supplementary Materials, Supplementary Figures 3 and 4). Although we obtained higher tSNR and stronger task-evoked responses in the brainstem nuclei (see Supplementary Figure 4 and Figure 4, respectively) for the 7 T acquisition, we are cautious with our interpretation of a (causal) relationship. The relationship between tSNR and BOLD-acquisition sensitivity is complex and nonlinear (Murphy, Bodurka, & Bandettini, 2007; Triantafyllou et al., 2005; Wald, 2012; Welvaert & Rosseel, 2013). TSNR combines non-neural (physiological and thermal) noise and genuine, ongoing neural variability (Fox & Raichle, 2007), which is also abundant in electrophysiological measurements of neural mass action (Hipp, Hawellek, Corbetta, Siegel, & Engel, 2012). Hence, we here focused on comparing the amplitude of evoked fMRI responses between field strengths, in a well-controlled task design with established neurophysiological underpinnings.

4 | DISCUSSION

Our current study focused on the comparison of field-strength dependence of evoked fMRI responses between different brain regions: in particular brainstem nuclei versus larger, easier to image structures, such as striatum and cortex. This focus was motivated by strong prior hypotheses regarding these responses across brain regions. We used an extensively studied cognitive task (visual perceptual decisions under uncertainty) to perform a systematic, within-subject, head-to-head comparison of evoked responses between 3 and 7 T fMRI acquisitions, across a range of well-defined cortical and subcortical brain regions. Overall, our findings are consistent with the notion that sensitivity for evoked responses in the small brainstem nuclei (during the decision interval and to a lesser extent also during the post-feedback interval) benefitted most from 7 T measurements.

We did not opt for an exact match of imaging parameters, in particular spatial resolution, between field strengths, but rather chose resolutions that would be common choices for each field strength (e.g., Hale et al., 2010; Morris et al., 2019; Theysohn et al., 2013; Torrisi et al., 2018). Accordingly, spatial resolution was higher for our 7 than 3 T measurements (see Section 2). Nonetheless, we obtained equally strong, or even stronger responses at 7 T, in particular in brainstem regions. This highlights the utility of 7 T measurements for high-precision fMRI, in particular in brainstem structures, the activity of which has been notoriously difficult to monitor with 3 T fMRI.

Other imaging parameters apart from spatial resolution also differed between our 3 and 7 T measurements, but we consider it unlikely that these differences have biased our current findings. The used TE at 3 T was somewhat longer than 7 T: still both TEs were rather short compared to the cortical gray matter T2* (Peters et al., 2007), especially at 3 T. This allows for whole-brain coverage and a reasonable TR and is wide-spread practice in cognitive neuroimaging. The SENSE factor, bandwidth and EPI factor contribute to differences in the amount of susceptibility-induced image distortion, but these differences are much smaller than those caused by the B0 difference. EPIs at 7 T are more distorted than those at 3 T, but both are corrected by B0-field unwarping and therefore should not have affected the BOLD measures. Finally, also the radio frequency (RF) coils differed between the 3 and 7 T measurements. Indeed, the properties of the RF coil significantly influence the SNR distribution over the brain (Wiggins et al., 2006). Yet, we used two state-of-the-art, vendor-provided coils offering whole-head coverage.

A recent study (de Hollander et al., 2017) concluded that common acquisition parameters (at higher field strength) may be optimized for specific brain regions, and, furthermore, that brain regions differ in terms of physiological noise contributions and distance from the receiver coils. The study did not find reliable hemodynamic responses in the brainstem's iron-rich nuclei during a robust stop-signal reaction task using "standard" 7 T imaging parameters. Successfully imaging the basal ganglia nuclei at 7 T required a shorter TE (~15 ms) as compared to cortex (25–35 ms), but also other factors interacted with signal detectability, for instance, the spatial resolution and acceleration factor. We note that although the iron-rich SN may suffer disproportionally from signal dropout at UHF strength (Torrisi et al., 2017), the task-evoked responses obtained in the present study were greater within the SN-ROI at 7 T as compared with 3 T.

The main interest of cognitive neuroimaging in 7 T fMRI lies in the ability to detect small-amplitude variations of brain activity even at high spatial resolution (Welvaert & Rosseel, 2013). For example, van der Zwaag et al. (2009) found that the number of activated voxels, t-statistics, and percent signal change all increased significantly with field strength (1.5, 3, and 7 T) in the same common ROI in a head-to-head comparison of six participants performing a simple motor task. Stronger bilateral hippocampus activation during memory encoding was obtained at 7 T fMRI as compared with 3 T (Theysohn et al., 2013). More recently, Torrisi et al. (2018) concluded that 7 T

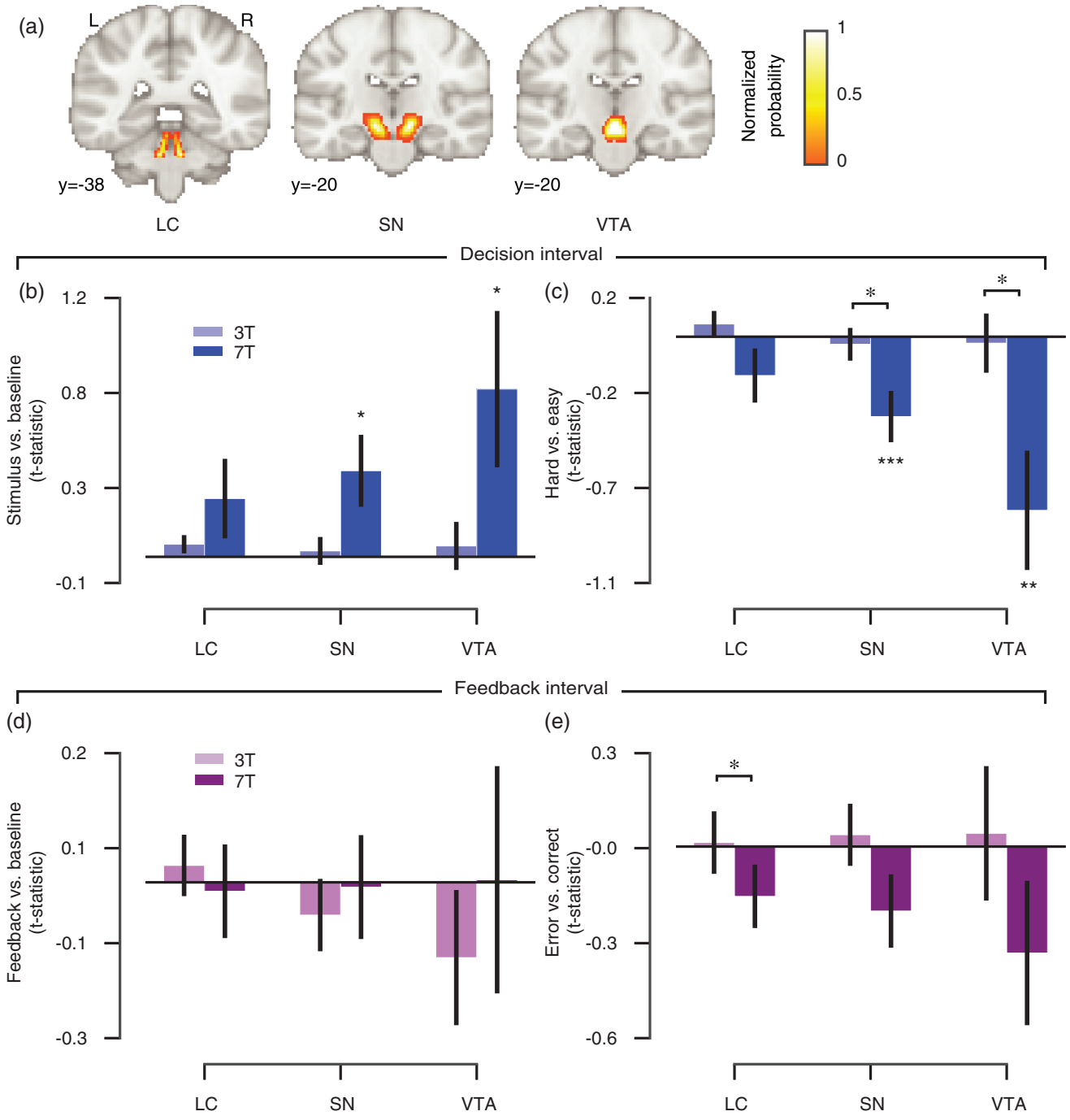

FIGURE 4 Planned comparisons of task-evoked responses for 3 and 7 T acquisitions in brainstem nuclei. (a) Brainstem masks are illustrated on the MNI152 brain. Each mask was rescaled between 0 and 1 (normalized probability). LC, locus coeruleus; SN, substantia nigra; VTA, ventral tegmental area. (b) Amplitude of evoked response per brainstem nucleus and field strength for the overall response within the decision interval (stimulus-locked and compared to the implicit baseline). (c) The amplitude difference between hard as compared with easy trials (decision interval). (d) Amplitude of evoked response per brainstem nucleus and field strength for the overall response within the feedback interval (feedback-locked and compared to the implicit baseline). (e) The amplitude difference between error as compared with correct trials (feedback interval). The 3 T amplitudes were averaged across 3 T-A and 3 T-B data subsets. Planned comparisons: $^{*}p < .05$, $^{**}p < .01$, $^{***}p < .001$ (two-tailed permutation tests). Error bars, *SEM* ($N = 8$)

fMRI resulted in significant gains compared to 3 T in terms of effect size, detection of smaller effects, and group-level power while measuring response inhibition (a standard GO/NOGO task). To our knowledge, the current study is the first that directly compared the benefits of 7 T fMRI field strength between cortical, striatal, and brainstem regions.

The differential responses in brainstem (in particular VTA/SN) during decision intervals we observed here were largely in line with a coding of confidence and/or reward anticipation, as observed in previous single-unit recordings from dopaminergic midbrain neurons in monkeys (Lak et al., 2017). Likewise, the differential responses to the feedback are in line with the coding of reward prediction errors and are also in line with Lak et al. (2017). Thus, our findings add to a growing body of literature implicating dopamine in perceptual decision-making under uncertainty (de Lafuente & Romo, 2011; Lak et al., 2017; Nomoto, Schultz, Watanabe, & Sakagami, 2010). Specifically, dopaminergic midbrain neurons encode not only prediction errors upon feedback about decision outcome, but they encode a graded "belief state" about the accuracy of a choice, given the evidence and choice (Lak et al., 2017); for indirect measurements in humans see (Colizoli et al., 2018; Urai et al., 2017). This graded belief state is analogous with a graded reward anticipation that evolves after (or even during) decision formation and is maintained until the delivery of feedback, evident in brainstem activity (Lak et al., 2017) as well as behavioral proxy variables (Colizoli et al., 2018; Urai et al., 2017).

The current study has some limitations. First, the number of subjects included in the study was relatively small, which may counteract the replicability of the results (Button et al., 2013; Ioannidis, 2005; Pashler & Harris, 2012; Pashler & Wagenmakers, 2012). Yet, our focus was on eliminating between-subject variability, a major factor in cognitive neuroscience studies, as a confound in the comparison between 3 and 7 T acquisitions. This required the testing of the same subjects in both scanners. We also took a number of measures to maximize replicability of the results within each subject and scanner. For each field strength, we collected a comparably large amount of data from the same participants within the main task at each field strength, yielding meaningful response estimates at the individual subject level (see also Smith & Little, 2018). We also assessed the data quality with an independent localizer scan (see Figure 2), and we assessed the test–retest reliability of the 3 T acquisitions across sessions (Supplementary Figure 5). We used an established decision-making task with well-characterized effects on behavior, arousal, and neuronal activity (at the single-neuron level). Second, the acquisition protocols did not entail simultaneous multiband acceleration. We opted for a standard excitation multislice EPI, because a multiband reconstruction, especially in combination with the in-plane acceleration used here, is known to lead to increased noise in the subcortex (Setsompop et al., 2012). The small difference in in-plane acceleration used here is not expected to lead to different amounts of g-factor noise across the ROIs for the current 32-channel coil (Hendriks, Luijten, Klomp, & Petridou, 2019; Wiggins et al., 2006). Third, RF-power optimization was done over the whole brain, which leads to overtipping in the center and undertipping in the temporal poles and cerebellum (Oliveira, Roos, Dumoulin, Siero, & van der Zwaag, 2021). This B1 inhomogeneity contributes to regional differences between evoked responses across the brain and may differ between field strengths. A field-strength dependent difference in B1 inhomogeneity was not accounted for in the current study and so may have contributed to the pattern of results obtained. By how much these and other limiting factors influence the benefit of 7 T imaging for brainstem regions remains an open question for future research.

5 | CONCLUSION

In conclusion, our results highlight the potential of 7 T fMRI for illuminating the contribution of subcortical structures, in particular small neuromodulatory brainstem nuclei, to cognition in the human brain. Computational theory (Dayan, 2012; Montague et al., 2004) and physiological evidence (e.g., Aston-Jones & Cohen, 2005; D'Ardenne et al., 2008; de Gee et al., 2017; Engelhard et al., 2019; Iglesias et al., 2013; Lak et al., 2017; Varazzani, San-Galli, Gilardeau, & Bouret, 2015) point to a key role of these brainstem structures in the orchestration of cognitive computations operating in higher-tier brain regions. Yet, progress in pinpointing their computational role, and in particular, their impact on the cortical networks implementing cognitive computations, has so far been limited. The main reason is the technical challenge entailed in monitoring the activity of small brainstem nuclei such as the VTA or LC with the necessary spatial precision and sensitivity. We envisage that the progressive establishment of 7 T fMRI in neuroimaging centers will lead to a surge of studies illuminating the role of the brainstem in cognition. This will not only deepen insight into healthy cognition, but also advance the mechanistic understanding of psychiatric disorders (Montague et al., 2004; Stephan et al., 2015).

ACKNOWLEDGMENTS

This work was carried out on the Dutch national e-infrastructure with the support of the SURF Cooperative (www.surfsara.nl). We thank Tomas Knapen for contributing analysis materials, and Birte U. Forstmann and Max C. Keuken for advice on the experimental design. Open Access funding enabled and organized by Projekt DEAL. [Correction added on 25 November 2021, after first online publication: Projekt Deal funding statement has been added.]

CONFLICT OF INTEREST

The authors declare no potential conflict of interests.

AUTHOR CONTRIBUTIONS

Olympia Colizoli: Contributed conceptualization, investigation, formal analysis, analysis materials, writing - original draft, writing – review and editing. **Jan Willem de Gee**: Contributed conceptualization, investigation, formal analysis, analysis materials, writing - review and editing. **Wietske van der Zwaag**: Contributed methodology, investigation, writing - review and editing. **Tobias H. Donner**: Contributed conceptualization, resources, supervision, writing - original draft, writing - review and editing.

DATA AVAILABILITY STATEMENT

The data and analysis code are publicly available (https://doi.org/10.17026/dans-zzd-nw4a) (Colizoli, de Gee, van der Zwaag, & Donner, 2021) and comply with the funding bodies' requirements.

PATIENT CONSENT

All participants signed a written informed consent form prior to participation.

ORCID

Olympia Colizoli https://orcid.org/0000-0001-5288-2437
Jan Willem de Gee https://orcid.org/0000-0002-5875-8282
Wietske van der Zwaag https://orcid.org/0000-0003-3223-9721
Tobias H. Donner https://orcid.org/0000-0002-7559-6019

REFERENCES

Aston-Jones, G., & Cohen, J. D. (2005). An integrative theory of locus coeruleus-norepinephrine function: Adaptive gain and optimal performance. *Annual Review of Neuroscience*, *28*, 403–450.

Ballard, I. C., Murty, V. P., Carter, R. M., MacInnes, J. J., Huettel, S. A., & Adcock, R. A. (2011). Dorsolateral prefrontal cortex drives mesolimbic dopaminergic regions to initiate motivated behavior. *The Journal of Neuroscience*, *31*, 10340–10346. https://doi.org/10.1523/JNEUROSCI.0895-11.2011

Beissner, F. (2015). Functional MRI of the brainstem: Common problems and their solutions. *Clinical Neuroradiology*, *25*, 251–257. https://doi.org/10.1007/s00062-015-0404-0

Beissner, F., Schumann, A., Brunn, F., Eisenträger, D., & Bär, K.-J. (2014). Advances in functional magnetic resonance imaging of the human brainstem. *NeuroImage*, *86*, 91–98. https://doi.org/10.1016/j.neuroimage.2013.07.081

Beisteiner, R., Robinson, S., Wurnig, M., Hilbert, M., Merksa, K., Rath, J., … Geissler, A. (2011). Clinical fMRI: Evidence for a 7T benefit over 3T. *NeuroImage*, *57*, 1015–1021. https://doi.org/10.1016/j.neuroimage.2011.05.010

Betts, M. J., Kirilina, E., Otaduy, M. C. G., Ivanov, D., Acosta-Cabronero, J., Callaghan, M. F., … Hämmerer, D. (2019). Locus coeruleus imaging as a biomarker for noradrenergic dysfunction in neurodegenerative diseases. *Brain*, *142*, 2558–2571. https://doi.org/10.1093/brain/awz193

Bode, S., He, A. H., Soon, C. S., Trampel, R., Turner, R., & Haynes, J.-D. (2011). Tracking the unconscious generation of free decisions using ultra-high field fMRI. *PLoS One*, *6*, e21612. https://doi.org/10.1371/journal.pone.0021612

Born, R. T., & Bradley, D. C. (2005). Structure and function of visual area MT. *Annual Review of Neuroscience*, *28*, 157–189. https://doi.org/10.1146/annurev.neuro.26.041002.131052

Braddick, O. J., O'Brien, J. M. D., Wattam-Bell, J., Atkinson, J., Hartley, T., & Turner, R. (2001). Brain areas sensitive to coherent visual motion. *Perception*, *30*, 61–72. https://doi.org/10.1068/p3048

Brainard, D. H. (1997). The psychophysics toolbox. *Spatial Vision*, *10*, 433–436. https://doi.org/10.1163/156856897X00357

Britten, K., Shadlen, M., Newsome, W., & Movshon, J. (1992). The analysis of visual motion: A comparison of neuronal and psychophysical performance. *The Journal of Neuroscience*, *12*, 4745. https://doi.org/10.1523/JNEUROSCI.12-12-04745.1992

Britten, K. H., Shadlen, M. N., Newsome, W. T., & Movshon, J. A. (1993). Responses of neurons in macaque MT to stochastic motion signals. *Visual Neuroscience*, *10*, 1157–1169. https://doi.org/10.1017/S0952523800010269

Brooks, J., Faull, O., Pattinson, K., & Jenkinson, M. (2013). Physiological noise in brainstem fMRI. *Frontiers in Human Neuroscience*, *7*, 623. https://doi.org/10.3389/fnhum.2013.00623

Button, K. S., Ioannidis, J. P., Mokrysz, C., Nosek, B. A., Flint, J., Robinson, E. S., & Munafò, M. R. (2013). Power failure: Why small sample size undermines the reliability of neuroscience. *Nature Reviews Neuroscience*, *14*, 365–376.

Colizoli, O., de Gee, J. W., Urai, A. E., & Donner, T. H. (2018). Task-evoked pupil responses reflect internal belief states. *Scientific Reports*, *8*, 13702. https://doi.org/10.1038/s41598-018-31985-3

Colizoli, O., de Gee, J. W., van der Zwaag, W., & Donner, T. H. (2021). *fMRI responses during perceptual decision-making at 3 and 7 Tesla in human cortex, striatum, and brainstem*. The Hague, Netherlands: Data Archiving and Networked Services (DANS). https://doi.org/10.17026/dans-zzd-nw4a

D'Ardenne, K., McClure, S. M., Nystrom, L. E., & Cohen, J. D. (2008). BOLD responses reflecting dopaminergic signals in the human ventral tegmental area. *Science*, *319*, 1264. https://doi.org/10.1126/science.1150605

Dayan, P. (2012). Twenty-five lessons from computational neuromodulation. *Neuron*, *76*, 240–256.

de Gee, J. W., Colizoli, O., Kloosterman, N. A., Knapen, T., Nieuwenhuis, S., & Donner, T. H. (2017). Dynamic modulation of decision biases by brainstem arousal systems. *eLife*, *6*, e23232. https://doi.org/10.7554/eLife.23232

de Hollander, G., Keuken, M. C., van der Zwaag, W., Forstmann, B. U., & Trampel, R. (2017). Comparing functional MRI protocols for small, iron-rich basal ganglia nuclei such as the subthalamic nucleus at 7 T and 3 T. *Human Brain Mapping*, *38*, 3226–3248. https://doi.org/10.1002/hbm.23586

de Lafuente, V., & Romo, R. (2011). Dopamine neurons code subjective sensory experience and uncertainty of perceptual decisions. *Proceedings of the National Academy of Sciences of the United States of America*, *108*, 19767. https://doi.org/10.1073/pnas.1117636108

Ding, L., & Gold, J. I. (2013). The basal ganglia's contributions to perceptual decision making. *Neuron*, *79*, 640–649. https://doi.org/10.1016/j.neuron.2013.07.042

Donner, T. H., Siegel, M., Oostenveld, R., Fries, P., Bauer, M., & Engel, A. K. (2007). Population activity in the human dorsal pathway predicts the accuracy of visual motion detection. *Journal of Neurophysiology*, *98*, 345–359.

Duong, T. Q., Yacoub, E., Adriany, G., Hu, X., Ugurbil, K., Vaughan, J. T., … Kim, S.-G. (2002). High-resolution, spin-echo BOLD, and CBF fMRI at 4 and 7 T. *Magnetic Resonance in Medicine*, *48*, 589–593. https://doi.org/10.1002/mrm.10252

Edelstein, W. A., Glover, G. H., Hardy, C. J., & Redington, R. W. (1986). The intrinsic signal-to-noise ratio in NMR imaging. *Magnetic Resonance in Medicine*, *3*, 604–618. https://doi.org/10.1002/mrm.1910030413

Efron, B., & Tibshirani, R. (1998). The problem of regions. *The Annals of Statistics*, *26*, 1687–1718. https://doi.org/10.1214/aos/1024691353

Engelhard, B., Finkelstein, J., Cox, J., Fleming, W., Jang, H. J., Ornelas, S., … Witten, I. B. (2019). Specialized coding of sensory, motor and cognitive variables in VTA dopamine neurons. *Nature*, *570*, 509–513. https://doi.org/10.1038/s41586-019-1261-9

Ernst, M. D. (2004). Permutation methods: A basis for exact inference. *Statistical Science*, *19*, 676–685. http://www.jstor.org/stable/4144438

Fox, M. D., & Raichle, M. E. (2007). Spontaneous fluctuations in brain activity observed with functional magnetic resonance imaging. *Nature Reviews Neuroscience*, *8*, 700–711. https://doi.org/10.1038/nrn2201

Glover, G. H., Li, T.-Q., & Ress, D. (2000). Image-based method for retrospective correction of physiological motion effects in fMRI: RETROICOR. *Magnetic Resonance in Medicine*, *44*, 162–167. https://doi.org/10.1002/1522-2594(200007)44:1<162::AID-MRM23>3.0.CO;2-E

Gold, J. I., & Shadlen, M. N. (2007). The neural basis of decision making. *Annual Review of Neuroscience*, *30*, 535–574.

Hale, J. R., Brookes, M. J., Hall, E. L., Zumer, J. M., Stevenson, C. M., Francis, S. T., & Morris, P. G. (2010). Comparison of functional connectivity in default mode and sensorimotor networks at 3 and 7T. *Magnetic Resonance Materials in Physics, Biology and Medicine*, *23*, 339–349. https://doi.org/10.1007/s10334-010-0220-0

Harvey, A. K., Pattinson, K. T. S., Brooks, J. C. W., Mayhew, S. D., Jenkinson, M., & Wise, R. G. (2008). Brainstem functional magnetic

resonance imaging: Disentangling signal from physiological noise. *Journal of Magnetic Resonance Imaging*, *28*, 1337–1344. https://doi.org/10.1002/jmri.21623

Harvey, B. M., Klein, B. P., Petridou, N., & Dumoulin, S. O. (2013). Topographic representation of Numerosity in the human parietal cortex. *Science*, *341*, 1123. https://doi.org/10.1126/science.1239052

Hayashi, M. J., van der Zwaag, W., Bueti, D., & Kanai, R. (2018). Representations of time in human frontoparietal cortex. *Communications Biology*, *1*, 233. https://doi.org/10.1038/s42003-018-0243-z

Hendriks, A. D., Luijten, P. R., Klomp, D. W. J., & Petridou, N. (2019). Potential acceleration performance of a 256-channel whole-brain receive array at 7 T. *Magnetic Resonance in Medicine*, *81*, 1659–1670. https://doi.org/10.1002/mrm.27519

Hipp, J. F., Hawellek, D. J., Corbetta, M., Siegel, M., & Engel, A. K. (2012). Large-scale cortical correlation structure of spontaneous oscillatory activity. *Nature Neuroscience*, *15*, 884–890. https://doi.org/10.1038/nn.3101

Huk, A. C., Dougherty, R. F., & Heeger, D. J. (2002). Retinotopy and functional subdivision of human areas MT and MST. *The Journal of Neuroscience*, *22*, 7195. https://doi.org/10.1523/JNEUROSCI.22-16-07195.2002

Huk, A. C., & Heeger, D. J. (2002). Pattern-motion responses in human visual cortex. *Nature Neuroscience*, *5*, 72–75. https://doi.org/10.1038/nn774

Iglesias, S., Mathys, C., Brodersen, K. H., Kasper, L., Piccirelli, M., den Ouden, H. E. M., & Stephan, K. E. (2013). Hierarchical prediction errors in midbrain and basal forebrain during sensory learning. *Neuron*, *80*, 519–530. https://doi.org/10.1016/j.neuron.2013.09.009

Ioannidis, J. P. A. (2005). Why most published research findings are false. *PLoS Medicine*, *2*, e124. https://doi.org/10.1371/journal.pmed.0020124

Jenkinson, M., Beckmann, C. F., Behrens, T. E., Woolrich, M. W., & Smith, S. M. (2012). Fsl. *NeuroImage*, *62*, 782–790. https://doi.org/10.1016/j.neuroimage.2011.09.015

Jones, T. B., Bandettini, P. A., & Birn, R. M. (2008). Integration of motion correction and physiological noise regression in fMRI. *NeuroImage*, *42*, 582–590. https://doi.org/10.1016/j.neuroimage.2008.05.019

Keren, N. I., Lozar, C. T., Harris, K. C., Morgan, P. S., & Eckert, M. A. (2009). In vivo mapping of the human locus coeruleus. *NeuroImage*, *47*, 1261–1267. https://doi.org/10.1016/j.neuroimage.2009.06.012

Lak, A., Nomoto, K., Keramati, M., Sakagami, M., & Kepecs, A. (2017). Midbrain dopamine neurons signal belief in choice accuracy during a perceptual decision. *Current Biology*, *27*, 821–832. https://doi.org/10.1016/j.cub.2017.02.026

Marques, J. P., & Norris, D. G. (2018). How to choose the right MR sequence for your research question at 7T and above? *NeuroImage*, *168*, 119–140. https://doi.org/10.1016/j.neuroimage.2017.04.044

Mestres-Missé, A., Turner, R., & Friederici, A. D. (2012). An anterior–posterior gradient of cognitive control within the dorsomedial striatum. *NeuroImage*, *62*, 41–47. https://doi.org/10.1016/j.neuroimage.2012.05.021

Montague, P. R., Hyman, S. E., & Cohen, J. D. (2004). Computational roles for dopamine in behavioural control. *Nature*, *431*, 760.

Morris, L. S., Kundu, P., Costi, S., Collins, A., Schneider, M., Verma, G., … Murrough, J. W. (2019). Ultra-high field MRI reveals mood-related circuit disturbances in depression: A comparison between 3-tesla and 7-tesla. *Translational Psychiatry*, *9*, 94. https://doi.org/10.1038/s41398-019-0425-6

Murphy, K., Bodurka, J., & Bandettini, P. A. (2007). How long to scan? The relationship between fMRI temporal signal to noise ratio and necessary scan duration. *NeuroImage*, *34*, 565–574. https://doi.org/10.1016/j.neuroimage.2006.09.032

Murty, V. P., Shermohammed, M., Smith, D. V., Carter, R. M., Huettel, S. A., & Adcock, R. A. (2014). Resting state networks distinguish human ventral tegmental area from substantia nigra. *NeuroImage*, *100*, 580–589. https://doi.org/10.1016/j.neuroimage.2014.06.047

Newsome, W., & Pare, E. (1988). A selective impairment of motion perception following lesions of the middle temporal visual area (MT). *The Journal of Neuroscience*, *8*, 2201. https://doi.org/10.1523/JNEUROSCI.08-06-02201.1988

Nomoto, K., Schultz, W., Watanabe, T., & Sakagami, M. (2010). Temporally extended dopamine responses to perceptually demanding reward-predictive stimuli. *The Journal of Neuroscience*, *30*, 10692. https://doi.org/10.1523/JNEUROSCI.4828-09.2010

Oliveira, Í. A. F., Roos, T., Dumoulin, S. O., Siero, J. C. W., & van der Zwaag, W. (2021). Can 7T MPRAGE match MP2RAGE for gray-white matter contrast? *NeuroImage*, *240*, 118384. https://doi.org/10.1016/j.neuroimage.2021.118384

Pashler, H., & Harris, C. R. (2012). Is the replicability crisis overblown? Three arguments examined. *Perspectives on Psychological Science*, *7*, 531–536. https://doi.org/10.1177/1745691612463401

Pashler, H., & Wagenmakers, E. (2012). Editors' introduction to the special section on replicability in psychological science: A crisis of confidence? *Perspectives on Psychological Science*, *7*, 528–530. https://doi.org/10.1177/1745691612465253

Peters, A. M., Brookes, M. J., Hoogenraad, F. G., Gowland, P. A., Francis, S. T., Morris, P. G., & Bowtell, R. (2007). T2* measurements in human brain at 1.5, 3 and 7 T. *Magnetic Resonance Imaging*, *25*, 748–753. https://doi.org/10.1016/j.mri.2007.02.014

Pohmann, R., Speck, O., & Scheffler, K. (2016). Signal-to-noise ratio and MR tissue parameters in human brain imaging at 3, 7, and 9.4 Tesla using current receive coil arrays. *Magnetic Resonance in Medicine*, *75*, 801–809. https://doi.org/10.1002/mrm.25677

Rees, G., Friston, K., & Koch, C. (2000). A direct quantitative relationship between the functional properties of human and macaque V5. *Nature Neuroscience*, *3*, 716–723. https://doi.org/10.1038/76673

Schäfer, A., van der Zwaag, W., Francis, S. T., Head, K. E., Gowland, P. A., & Bowtell, R. W. (2007). High resolution SE-fMRI in humans at 3 and 7 T using a motor task. *Magnetic Resonance Materials in Physics, Biology and Medicine*, *21*, 113. https://doi.org/10.1007/s10334-007-0099-6

Sclocco, R., Beissner, F., Bianciardi, M., Polimeni, J. R., & Napadow, V. (2018). Challenges and opportunities for brainstem neuroimaging with ultrahigh field MRI. *NeuroImage*, *168*, 412–426. https://doi.org/10.1016/j.neuroimage.2017.02.052

Setsompop, K., Cohen-Adad, J., Gagoski, B. A., Raij, T., Yendiki, A., Keil, B., … Wald, L. L. (2012). Improving diffusion MRI using simultaneous multi-slice echo planar imaging. *NeuroImage*, *63*, 569–580. https://doi.org/10.1016/j.neuroimage.2012.06.033

Siegel, M., Donner, T. H., Oostenveld, R., Fries, P., & Engel, A. K. (2006). High-frequency activity in human visual cortex is modulated by visual motion strength. *Cerebral Cortex*, *17*, 732–741. https://doi.org/10.1093/cercor/bhk025

Siegel, M., Engel, A. K., & Donner, T. H. (2011). Cortical network dynamics of perceptual decision-making in the human brain. *Frontiers in Human Neuroscience*, *5*, 1–12. https://doi.org/10.3389/fnhum.2011.00021

Smith, P. L., & Little, D. R. (2018). Small is beautiful: In defense of the small-N design. *Psychonomic Bulletin & Review*, *25*, 2083–2101. https://doi.org/10.3758/s13423-018-1451-8

Smith, S. M., Jenkinson, M., Woolrich, M. W., Beckmann, C. F., Behrens, T. E., Johansen-Berg, H., … Flitney, D. E. (2004). Advances in functional and structural MR image analysis and implementation as FSL. *NeuroImage*, *23*, S208–S219. https://doi.org/10.1016/j.neuroimage.2004.07.051

Stephan, K. E., Iglesias, S., Heinzle, J., & Diaconescu, A. O. (2015). Translational perspectives for computational neuroimaging. *Neuron*, *87*, 716–732. https://doi.org/10.1016/j.neuron.2015.07.008

Theysohn, N., Qin, S., Maderwald, S., Poser, B. A., Theysohn, J. M., Ladd, M. E., … Tendolkar, I. (2013). Memory-related hippocampal activity can be measured robustly using fMRI at 7 Tesla. *Journal of Neuroimaging*, *23*, 445–451. https://doi.org/10.1111/jon.12036

Thürling, M., Hautzel, H., Küper, M., Stefanescu, M. R., Maderwald, S., Ladd, M. E., & Timmann, D. (2012). Involvement of the cerebellar cortex and nuclei in verbal and visuospatial working memory: A 7T fMRI study. *NeuroImage*, *62*, 1537–1550. https://doi.org/10.1016/j.neuroimage.2012.05.037

Thürling, M., Küper, M., Stefanescu, R., Maderwald, S., Gizewski, E. R., Ladd, M. E., & Timmann, D. (2011). Activation of the dentate nucleus in a verb generation task: A 7T MRI study. *NeuroImage*, *57*, 1184–1191. https://doi.org/10.1016/j.neuroimage.2011.05.045

Tootell, R., Reppas, J., Kwong, K., Malach, R., Born, R., Brady, T., … Belliveau, J. (1995). Functional analysis of human MT and related visual cortical areas using magnetic resonance imaging. *The Journal of Neuroscience*, *15*, 3215. https://doi.org/10.1523/JNEUROSCI.15-04-03215.1995

Tootell, R. B. H., Mendola, J. D., Hadjikhani, N. K., Ledden, P. J., Liu, A. K., Reppas, J. B., … Dale, A. M. (1997). Functional analysis of V3A and related areas in human visual cortex. *The Journal of Neuroscience*, *17*, 7060. https://doi.org/10.1523/JNEUROSCI.17-18-07060.1997

Torrisi, S., Chen, G., Glen, D., Bandettini, P. A., Baker, C. I., Reynolds, R., … Ernst, M. (2018). Statistical power comparisons at 3T and 7T with a GO/NOGO task. *NeuroImage*, *175*, 100–110. https://doi.org/10.1016/j.neuroimage.2018.03.071

Torrisi, S., Nord, C. L., Balderston, N. L., Roiser, J. P., Grillon, C., & Ernst, M. (2017). Resting state connectivity of the human habenula at ultra-high field. *NeuroImage*, *147*, 872–879. https://doi.org/10.1016/j.neuroimage.2016.10.034

Triantafyllou, C., Hoge, R. D., Krueger, G., Wiggins, C. J., Potthast, A., Wiggins, G. C., & Wald, L. L. (2005). Comparison of physiological noise at 1.5 T, 3 T and 7 T and optimization of fMRI acquisition parameters. *NeuroImage*, *26*, 243–250. https://doi.org/10.1016/j.neuroimage.2005.01.007

Turner, R., Jezzard, P., Wen, H., Kwong, K. K., Le Bihan, D., Zeffiro, T., & Balaban, R. S. (1993). Functional mapping of the human visual cortex at 4 and 1.5 Tesla using deoxygenation contrast EPI. *Magnetic Resonance in Medicine*, *29*, 277–279. https://doi.org/10.1002/mrm.1910290221

Urai, A. E., Braun, A., & Donner, T. H. (2017). Pupil-linked arousal is driven by decision uncertainty and alters serial choice bias. *Nature Communications*, *8*, 14637. https://doi.org/10.1038/ncomms14637

van der Zwaag, W., Da Costa, S. E., Zürcher, N. R., Adams, R. B., & Hadjikhani, N. (2012). A 7 Tesla fMRI study of amygdala responses to fearful faces. *Brain Topography*, *25*, 125–128. https://doi.org/10.1007/s10548-012-0219-0

van der Zwaag, W., Francis, S., Head, K., Peters, A., Gowland, P., Morris, P., & Bowtell, R. (2009). fMRI at 1.5, 3 and 7 T: Characterising BOLD signal changes. *NeuroImage*, *47*, 1425–1434. https://doi.org/10.1016/j.neuroimage.2009.05.015

van der Zwaag, W., Schäfer, A., Marques, J. P., Turner, R., & Trampel, R. (2016). Recent applications of UHF-MRI in the study of human brain function and structure: A review. *NMR in Biomedicine*, *29*, 1274–1288. https://doi.org/10.1002/nbm.3275

Varazzani, C., San-Galli, A., Gilardeau, S., & Bouret, S. (2015). Noradrenaline and dopamine neurons in the reward/effort trade-off: A direct electrophysiological comparison in behaving monkeys. *The Journal of Neuroscience*, *35*, 7866. https://doi.org/10.1523/JNEUROSCI.0454-15.2015

Wald, L. L. (2012). The future of acquisition speed, coverage, sensitivity, and resolution. *NeuroImage*, *62*, 1221–1229. https://doi.org/10.1016/j.neuroimage.2012.02.077

Wang, L., Mruczek, R. E. B., Arcaro, M. J., & Kastner, S. (2014). Probabilistic maps of visual topography in human cortex. *Cerebral Cortex*, *25*, 3911–3931. https://doi.org/10.1093/cercor/bhu277

Welvaert, M., & Rosseel, Y. (2013). On the definition of signal-to-noise ratio and contrast-to-noise ratio for fMRI data. *PLoS One*, *8*, e77089. https://doi.org/10.1371/journal.pone.0077089

Wiggins, G. C., Triantafyllou, C., Potthast, A., Reykowski, A., Nittka, M., & Wald, L. L. (2006). 32-channel 3 Tesla receive-only phased-array head coil with soccer-ball element geometry. *Magnetic Resonance in Medicine*, *56*, 216–223. https://doi.org/10.1002/mrm.20925

Woolrich, M. W., Jbabdi, S., Patenaude, B., Chappell, M., Makni, S., Behrens, T., … Smith, S. M. (2009). Bayesian analysis of neuroimaging data in FSL. *NeuroImage*, *45*, S173–S186. https://doi.org/10.1016/j.neuroimage.2008.10.055

Woolrich, M. W., Ripley, B. D., Brady, M., & Smith, S. M. (2001). Temporal autocorrelation in univariate linear modeling of FMRI data. *NeuroImage*, *14*, 1370–1386. https://doi.org/10.1006/nimg.2001.0931

Yacoub, E., Duong, T. Q., Van De Moortele, P.-F., Lindquist, M., Adriany, G., Kim, S.-G., … Hu, X. (2003). Spin-echo fMRI in humans using high spatial resolutions and high magnetic fields. *Magnetic Resonance in Medicine*, *49*, 655–664. https://doi.org/10.1002/mrm.10433

Yacoub, E., Shmuel, A., Pfeuffer, J., Van De Moortele, P.-F., Adriany, G., Andersen, P., … Hu, X. (2001). Imaging brain function in humans at 7 Tesla. *Magnetic Resonance in Medicine*, *45*, 588–594. https://doi.org/10.1002/mrm.1080

SUPPORTING INFORMATION

Additional supporting information may be found in the online version of the article at the publisher's website.

How to cite this article: Colizoli, O., de Gee, J. W., van der Zwaag, W., & Donner, T. H. (2022). Functional magnetic resonance imaging responses during perceptual decision-making at 3 and 7 T in human cortex, striatum, and brainstem. *Human Brain Mapping*, *43*(4), 1265–1279. https://doi.org/10.1002/hbm.25719